Preliminary study of plasma modes and electron-ion collisions in partially magnetized strongly coupled plasmas

Chanhyun Pak, Virginia Billings,* Matthew Schlitters, and Scott D. Bergeson†
Department of Physics and Astronomy, Brigham Young University, Provo, Utah 84602, USA

Michael S. Murillo

Department of Computational Mathematics, Science and Engineering, Michigan State University, East Lansing, Michigan 48824, USA

Magnetic fields influence ion transport in plasmas. Straightforward comparisons of experimental measurements with plasma theories are complicated when the plasma is inhomogeneous, far from equilibrium, or characterized by strong gradients. To better understand ion transport in a partially magnetized system, we study the hydrodynamic velocity and temperature evolution in an ultracold neutral plasma at intermediate values of the magnetic field. We observe a transverse, radial breathing mode that does not couple to the longitudinal velocity. The inhomogeneous density distribution gives rise to a shear velocity gradient that appears to be only weakly damped. This mode is excited by ion oscillations originating in the wings of the distribution where the plasma becomes non-neutral. The ion temperature shows evidence of an enhanced electron-ion collision rate in the presence of the magnetic field. Ultracold neutral plasmas provide a rich system for studying mode excitation and decay.

I. INTRODUCTION

Magnetic fields and plasmas are often found together. In some cases, the magnetic field is applied to the plasma to confine the plasma or influence its dynamical properties [1–6]. In other cases, the fields are generated by the plasmas themselves and become an embedded characteristic of the system as it evolves [7–14]. Understanding how magnetic fields change transport properties is an integral part of high-fidelity multiscale plasma modeling for applications such as optimizing plasma confinement [2,15–19], understanding turbulence [20–22], or probing magnetic reconnection [23].

Magnetic fields allow new kinds waves [24] and modify dispersion relations [25]. When collisions are important, transport. coefficients themselves may depend on the magnetic field [26,27], modifying descriptions of diffusion, viscosity, and temperature relaxation [28–42]. Transport coefficients are determined by measuring gradients in temperature, density, and velocity and the fluxes that they drive.

Isolating and identifying a single transport process in experimental plasmas is extremely challenging [43]. Ultracold neutral plasmas (UNPs) offer the possibility of not only scuplting the initial density [44] but also systematically varying the density, independently adjusting the initial electron and ion temperatures [45–47], and choosing the ionization state [48], as many recent results demonstrate [42,49–55]. UNPs are strongly coupled, nondegenerate, quasihomogeneous, quasi-steady-state plasmas [45,46]. They simulate high energy-density plasmas over a limited range of parameters [49,56–64]. UNPs have been used to study instabilities [65], RF heating rates [66], and plasma confinement [5,67–69]. They are part of a constellation of low-density, low-temperature, complex plasmas including non-neutral [70–72] and dusty plasmas [6,73].

In this paper, we explore ion transport in an expanding, partially magnetized UNP more closely. Rather than measuring the plasma size vs time as in previous studies [42,55], we focus on the hydrodynamic velocity. Surprisingly, we observe a transverse radial breathing mode in the presence of a magnetic field that does not couple to the longitudinal ion motion. This mode is not readily detectable when measuring the transverse plasma size. The mode frequency scales with plasma non-neutrality, evidently driven by ion acoustic waves originating in the wings of the density distribution, where the plasma is no longer neutral [74]. We also observe enhanced electron-ion heating in the presence of the field. These data illustrate how UNPs provide a novel platform for studying mode excitation and relaxation.

II. UNP EXPANSION

When UNPs are created by photoionizing laser-cooled atoms in a magneto-optical trap, the initial ion spatial density is often spherically symmetric and Gaussian. For free

---

*Department of Physics and Astronomy, University of Rochester, Rochester, NY 14627.

†scott.bergeson@byu.edu

expansion into the vacuum, the expansion is self-similar, of the form,

$$n_i(r, t) = n_0 \exp[-r^2/2\sigma^2(t)], \tag{1}$$

where n_0 is the peak ion density, $\sigma(t) = \sigma_0(1 + t^2/\tau^2)^{1/2}$ is the RMS size of the plasma, $\tau^2 = (m_i\sigma_0^2)/[k_B(T_e(0) + T_i(0)]$, τ is a characteristic expansion time, m_i is the ion mass, and $T_e(0)$ and $T_i(0)$ are the initial electron and ion temperatures, respectively.

These UNPs are not strictly charge neutral. The non-neutrality, $\delta \equiv 1 - (N_e/N_i)$, was shown to be $\delta = \lambda_D/\sigma_0$, where N_α is the number of species α and $\lambda_D = [\epsilon_0 k_B T_e/(n_0 e^2)]^{1/2}$ is the electron Debye length in the center of the plasma [75–77]. However, non-neutrality is confined to the wings of the density distribution [74]. In the cold plasma approximation, the electron density distribution is

$$\frac{n_e^{(0)}(r)}{n_0} = \exp\left(-\frac{r^2}{2\sigma^2}\right) \begin{cases} 1, & r \leqslant R, \\ 0, & r > R. \end{cases} \tag{2}$$

When Eq. (1) is a good approximation of the ion density, the UNP charge imbalance is calculated as

$$\delta = 1 - \frac{1}{(2\pi\sigma^2)^{3/2}n_0} \int_0^R 4\pi r^2 n_i \, dr$$

$$= 1 + \frac{R}{\sigma}\sqrt{\frac{2}{\pi}} \exp\left(-\frac{R^2}{2\sigma^2}\right) - \text{erf}\left(\frac{R}{\sigma\sqrt{2}}\right). \tag{3}$$

The expansion described by Eq. (1) is driven by electron pressure [78]. However, a uniform external magnetic field reduces the transverse electron pressure, significantly changing the expansion properties [42,55]. The importance of the magnetic field can be understood in terms of a heirarchy of length and timescales. For our UNP work, typical plasma characteristics are $T_e = 100$ K, $T_i = 1$ K, $n_0 = 6 \times 10^8$ cm^{-3}, $\sigma_0 = 1.3$ mm, and $B = 100$ G. The electron Debye length, electron Larmor radius, and Wigner-Seitz radius are

$$\lambda_D = \left(\frac{\epsilon_0 k_B T_e}{ne^2}\right)^{1/2} = 26 \ \mu\text{m},$$

$$r_L = \frac{m_e v_{\text{th}}}{eB} = 22 \ \mu\text{m}, \tag{4}$$

$$a_{\text{ws}} = \left(\frac{3}{4\pi\epsilon_0}\right)^{1/3} = 7 \ \mu\text{m},$$

where $v_{\text{th}} = (k_B T_e/m_c)^{1/2}$, yielding the relation

$$\sigma_0 \gg \lambda_D \approx r_L > a_{\text{ws}}. \tag{5}$$

The electron cyclotron frequency, electron plasma frequency, and electron-ion collision rate are

$$\omega_c^{(e)} = \frac{eB}{m_e} = 2\pi \times 280 \text{ MHz},$$

$$\omega_p^{(e)} = \left(\frac{ne^2}{m_e\epsilon_0}\right)^{1/2} = 2\pi \times 230 \text{ MHz}, \tag{6}$$

$$\gamma_{ei} = \sqrt{\frac{2}{3\pi}}\Gamma_e^{3/2}\omega_p^{(e)} \ln\left[\frac{1}{\Gamma_e^{3/2}\sqrt{3}}\right] = 2\pi \times 2 \text{ MHz},$$

where $\Gamma_e = e^2/(4\pi\epsilon_0 a_{\text{ws}}k_B T_e)$ and γ_{ei} is calculated using the peak plasma density. This yields the relation

$$\omega_c^{(e)} \approx \omega_p^{(e)} \gg \gamma_{ei}. \tag{7}$$

The electrons move freely along the magnetic field lines and orbit them tightly in the transverse direction, experiencing infrequent collisions with UNP ions. Because the measurement window is only 50 μs, the magnetic field has almost no direct influence on the ion motion. The degree of magnetization for species α is characterized by the ratio of the cyclotron frequency to the plasma frequency, $\beta_\alpha = \omega_c^{(\alpha)}/\omega_p^{(\alpha)}$. For electrons and Ca$^+$ ions at a density of 6×10^8 cm^{-3} in a field of 100 G,

$$\beta_e = 1.3, \quad \beta_i = 0.005, \tag{8}$$

quantifying the field's strong influence on electronic motion and its vanishing influence on the ions.

III. UNP EXPANSION IN REDUCED DIMENSIONS

With Eq. (8) in mind, we adapt the expansion models of Refs. [58,79,80] to include the effect of the magnetic field on the plasma expansion. Rather than including the Lorentz force on the electrons explicitly, we include its effect phenomenologically by allowing the transverse expansion to proceed more slowly, corresponding to reduced transverse electron pressure. This model assumes exact charge neutrality, in conflict with Eq. (2). However, the model closely describes the expansion of UNPs in the absence of a magnetic field [58]. Because the non-neutrality is small and limited to the wings of the spatial distribution, this model is expected to be valid near the center of the plasma.

Using a self-similar Gaussian spatial distribution [42], and allowing for a generalized asymmetry in both size and expansion rate, we write the ion distribution function as

$$f_i = \frac{N_i}{8\pi^3\sigma_1\sigma_2\sigma_3 v_{\text{th}}^3} \exp\left(-\frac{x^2}{2\sigma_1^2} - \frac{y^2}{2\sigma_2^2} - \frac{z^2}{2\sigma_3^2}\right)$$

$$\times \exp\left[-\frac{(\vec{v} - \vec{u})^2}{2v_{\text{th}}^2}\right], \tag{9}$$

$$\vec{u} = \gamma_1 x\hat{i} + \gamma_2 y\hat{j} + \gamma_3 z\hat{k}, \tag{10}$$

where the rms widths $\sigma_1, \sigma_2, \sigma_3$, and $v_{\text{th}} = (k_B T_i/m_i)^{1/2}$ and the hydrodynamic velocity gradients γ_1, γ_2, and γ_3 all depend on time but not space, T_i is the ion temperature, and m_i is the ion mass.

The continuity equation,

$$\partial_t n_i + \nabla \cdot (n_i \vec{u}) = 0 \tag{11}$$

describes the evolution of the spatial density,

$$n_i = \int f_i \, d^3v, \tag{12}$$

in the absence of sources. For the distribution in Eq. (9), the continuity equation is

$$\frac{1}{\sigma_1}\left(1 - \frac{x^2}{\sigma_1^2}\right)(\gamma_1\sigma_1 - \partial_t\sigma_1)$$

$$+ \frac{1}{\sigma_2}\left(1 - \frac{y^2}{\sigma_2^2}\right)(\gamma_2\sigma_2 - \partial_t\sigma_2)$$

$$+ \frac{1}{\sigma_3}\left(1 - \frac{z^2}{\sigma_3^2}\right)(\gamma_3\sigma_3 - \partial_t\sigma_3) = 0, \qquad (13)$$

for which the only nontrivial solution is

$$\dot{\sigma}_k = \gamma_k\sigma_k, \qquad (14)$$

with $k = 1, 2, 3$.

The ion momentum equation is

$$m_i n_i[\partial_t\vec{u} + (\vec{u} \cdot \nabla)\vec{u}] = -k_B T_e\nabla n_i - \nabla P_{\text{th},i} + n_i\vec{F}_{ii}, \quad (15)$$

where $P_{\text{th},i}$ is the ion thermal pressure and $\vec{F}_{ii}$ is the "ion-ion correlation force" or the excess force arising from the ion-ion correlation function g_{ii} [79]. The ion thermal pressure is defined using an ideal gas law,

$$P_{\text{th},i} = \frac{m_i}{3}\int(\vec{v} - \vec{u})^2 f_i\,d^3v = n_i k_B T_i, \qquad (16)$$

due to the assumed Maxwellian nature of the velocity distribution. The ion-ion correlation force, described in Ref. [79], can be expressed as

$$n_i\vec{F}_{ii} = -\frac{1}{3}\left[\frac{\partial(u_{ii}n_i)}{\partial n_i}\right]\nabla n_i$$

$$= \frac{U_{ii}}{3}\left(\frac{x}{\sigma_1^2}\hat{i} + \frac{y}{\sigma_2^2}\hat{j} + \frac{z}{\sigma_3^2}\hat{k}\right)n_i, \qquad (17)$$

where U_{ii} is the ion-ion correlation energy. Therefore, Eq. (15) has the solution

$$\dot{\gamma}_k = \frac{k_B T_e + k_B T_i + U_{ii}/3}{m_i\sigma_k^2} - \gamma_k^2, \qquad (18)$$

provided that T_i has no spatial dependence.

The conservation of energy gives us an equation for the ion temperature. Equation (6c) in Ref. [79] can be written as

$$\frac{m_i}{2N_i}\partial_t\langle v^2\rangle = -\frac{k_B T_e}{N_i}\int(\nabla n_i)\cdot\vec{u}\,d^3r - \partial_t U_{ii}. \qquad (19)$$

This evaluates to

$$\frac{3}{2}k_B\dot{T}_i + (k_B T_e + k_B T_i + U_{ii}/3)\sum_{k=1}^{3}\gamma_k = k_B T_e\sum_{k=1}^{3}\gamma_k - \dot{U}_{ii}, \qquad (20)$$

yielding the ion temperature equation,

$$k_B\dot{T}_i = -\frac{2}{3}(k_B T_i + U_{ii}/3)\left(\sum_{k=1}^{3}\gamma_k\right) - \frac{2}{3}\dot{U}_{ii}. \qquad (21)$$

Including the effect of electron-ion collisions, as in Ref. [58] modifies the ion temperature equation,

$$k_B\dot{T}_i = -\frac{2}{3}(k_B T_i + U_{ii}/3)\left(\sum_{k=1}^{3}\gamma_k\right)$$

$$- \frac{2}{3}\dot{U}_{ii} + 2\frac{m_e}{m_i}\gamma_{ei}k_B(T_e - T_i), \qquad (22)$$

where m_e is the electron mass and γ_{ei} is the electron-ion collision frequency.

The electron temperature equation follows from the ion temperature equation. We recognize the first right-hand side term in Eq. (22) as adiabatic expansion. Neglecting electron-ion recombination and electron-electron correlation energy, both assumed to be small, and assuming charge neutrality and a Maxwellian electron velocity distribution, the electron temperature evolution is

$$k_B\dot{T}_e = -\frac{2}{3}(k_B T_i)\left(\sum_{k=1}^{3}\gamma_k\right) - 2\frac{m_e}{m_i}\gamma_{ei}k_B(T_e - T_i). \qquad (23)$$

Equations (14), (18) (22), and (23) form a set of coupled ordinary differential equations describing the plasma expansion. We solve these numerically using expressions in Appendix to determine $T_i(t)$ and $\gamma_k(t)$.

The magnetic field causes the expansion to become one dimensional. It was shown in Ref. [42] that for magnetic fields above a few hundred Gauss, the asymptotic transverse expansion velocity falls exponentially to zero. The magnetic field produces an external force on the electrons. We therefore consider the case when the gradient functions $\gamma_1(t)$ and $\gamma_2(t)$ are zero and the rms size distributions $\sigma_1(t)$ and $\sigma_2(t)$ are constants in time. Compared to the three-dimensional symmetric expansion, the velocity gradient $\gamma_3(t)$ is nearly unchanged. However, the ion temperature will fall more slowly.

The effect of non-neutrality on these model predictions is not obvious. Neutrality is implied in deriving the electron distribution and the properties of the plasma mean field. While neutrality is an excellent assumption in the center of the plasma, edge effects are explicitly not included. As we will see, these effects play a significant role in the plasma evolution.

IV. EXPERIMENT

We trap up to 20 million neutral Ca atoms in a MOT using 423-nm laser beams [42,50,57] and repumping at 424 nm [81] [see Fig. 1(a)]. The Ca^+ plasma is formed by ionizing the Ca atoms using 5-ns duration laser pulses at 423 and 390 nm, driving the $4s^2\,^1S_0 \to 4s4p\,^1P_1$ and $4s4p\,^1P_1 \to$ continuum transitions, respectively. The photon energy of the 390-nm laser above the ionization energy controls the electron temperature, T_e, with initial values ranging from 30 to 400 K.

We apply a constant uniform magnetic bias field in the z direction. Calculations indicate that the magnetic field varies by less than 1% across the spatial extent of the plasma. The MOT fields turn off coincident with the bias field turning on 1.4 ms before the ionization pulses, as shown in Fig. 1(c). This allows the neutral atom cloud to expand, reducing the peak
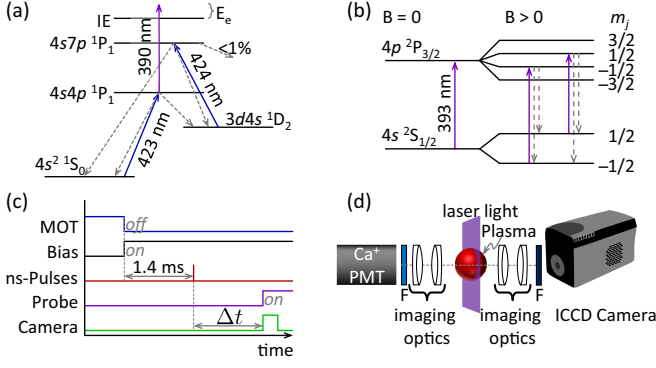
FIG. 1. (a) Partial energy level diagram for Ca. The number of atoms in the MOT is enhanced by repumping at 424 nm. Less than 1% of the population from the $4s7s\,^1P_1$ level is lost to the trap. (b) Energy levels in Ca$^+$. To avoid optically pumping, both $\Delta m = 0$ transitions are driven by the 393-nm probe laser light. (c) Timing diagram for the experiment. The MOT laser beams and magnetic field gradient are turned off, and a uniform bias field is turned on 1.4 ms before the ionizing laser pulse arrives. After a time Δt, the probe laser beams are turned on and the camera observes the laser-induced fluorescence. (d) Schematic representation of the fluorescence measurement geometry.

density and smoothing out the spatial distribution. We probe the ion velocity distribution by shining a 1-mm-thick sheet of 393 nm "probe" laser beam onto the plasma [82], driving both $4s\,^2S_1/2 - 4p\,^2P_3/2$ $\Delta m = 0$ transitions as shown in Fig. 1(b). For times up to $\Delta t = 50\,\mu$s after ionization, we measure laser-induced Ca$^+$ fluorescence in a 200- to 2000-ns duration time window. To prevent optical pumping into the ^2D states during the longer observation windows, we use lasers at 850 and 854 nm to empty the $3d\,^2D$ states. The initial density of the plasma is determined by fitting the zero-bias-field kinetic energy oscillation [83], and this is most conveniently done using the PMT signal. The initial plasma size is determined from fluorescence images. To a good approximation, the initial plasma spatial density profile is Gaussian, $n(r) = n_0 \exp[-r^2/(2\sigma_0)^2]$. Typical experimental values of the initial rms size and peak density are $\sigma_0 = 0.8$ to 1.5 mm, and $n_0 = 0.1$ to 1×10^9 cm^{-3}.

The probe laser beam illuminates a central 1-mm-thick slice of the plasma distribution, as shown in Fig. 1(d). The density variation over this width is less than $\pm 10\%$. When measuring the transverse ion velocity, we observe the fluorescence in a direction orthogonal to both the laser beam propagation direction and the magnetic field direction. Fluorescence from the plasma is optically filtered and imaged onto an ICCD camera using a 1:1 imaging system, discussed in the Supplemental Material [84,85]. Fluorescence images are recorded for typically 11 different probe laser frequency detunings, equally spaced across the Doppler- and Zeeman-shifted velocity profile. We collect fluorescence images at specific delay times after plasma formation, Δt_d, ranging from 0.1 to 50 µs. These data give us a two-dimensional image of the ion distribution function in the middle of the plasma at a specific time. Analysis of these images provides information on both the width of the velocity distribution and the spatially dependent hydrodynamic velocity.

V. DATA ANALYSIS

The fluorescence intensity is proportional to the number of ions in resonance with the probe laser beam at a particular time and position in the plasma. Together, the 11 fluorescence images can be analyzed pixel by pixel to determine the ion temperature and hydrodynamic expansion velocity. The fluorescence in each pixel, S, is fit to a Voigt profile as a function of the laser frequency, f_ℓ, detuned from the Doppler-shifted atomic resonance f_0,

$$S(x, z, f_\ell) = \int \frac{n(x, z)\pi\gamma_L}{[w - (f_0 - f_\ell)]^2 + \gamma_L^2}$$
$$\times \frac{1}{f_{rms}\sqrt{2\pi}} \exp\left[-\frac{w^2}{2f_{rms}^2}\right] dw \qquad (24)$$

where $n(x, z)$, f_{rms}, and f_0 are fit parameters. The Lorentzian half-width, γ_L, is assumed to be half of the power-broadened natural width of the $4s\,^2S_{1/2}$-$4p\,P_{3/2}$ level, $\gamma_L = (4\pi\tau)^{-1}\sqrt{1 + s} = 11.49$ MHz$\sqrt{1 + s}$, where $\tau_a = 6.924(0.019)$ ns is the excited state radiative lifetime [86], $s = I/I_{sat}$ is the saturation parameter, and $I_{sat} = (\pi hc)/(3\lambda^3\tau_a) = 50$ mW/cm^2. Typical values in these measurements are I/I_{sat} in the range of 0.1 to 0.5. The Gaussian rms frequency, f_{rms} is related to the thermal velocity through the Doppler shift, $v_{th} = \lambda f_{rms}$, and the ion temperature is

$$k_B T_i = m_i(\lambda f_{rms})^2, \qquad (25)$$

where $\lambda = 393$ nm is the wavelength of the ion transition.

All three fit parameters, $n(x, z)$, f_{rms}, and f_0, are two-dimensional matrices. They contain information about the number of ions, the thermal velocity, and the hydrodynamic velocity in the plane illuminated by the probe laser beam. Because of the Doppler shift, the fitted center frequency of the fluorescence peak, $f_0(x, z)$, only yields the component of the velocity in the direction parallel to the probe laser beam propagation.

In the direction parallel to the magnetic field, we show the time evolution of γ_3 and T_i in Fig. 2. The data in Fig. 2(a) show that the measured velocity gradient qualitatively follows the asymmetric expansion model. However, the ion temperature does not. After the initial disorder-induced heating phase at times less than 1 µs, the ion temperature is higher than expected, revealing an additional source of heating.

In the transverse direction, two-dimensional false color images of the ion temperature and hydrodynamic velocity are shown in Fig. 3. In these images, the probe laser propagates from left to right (the x direction) and the magnetic field points upwards (the z direction). In the absence of a magnetic field, the hydrodynamic velocity closely matches the predictions of a Vlasov model for Gaussian distribution functions [45], and the velocity gradient in the center of the plasma is highly linear in space. However, when a magnetic field is applied, transverse modes appear, as shown in Fig. 3.

The frequency of the mode depends on the initial electron temperature. In Fig. 4 we plot the gradient of the ion velocity in the center of the plasma. Although the transverse velocity gradient at the earliest time is small and positive, similar to
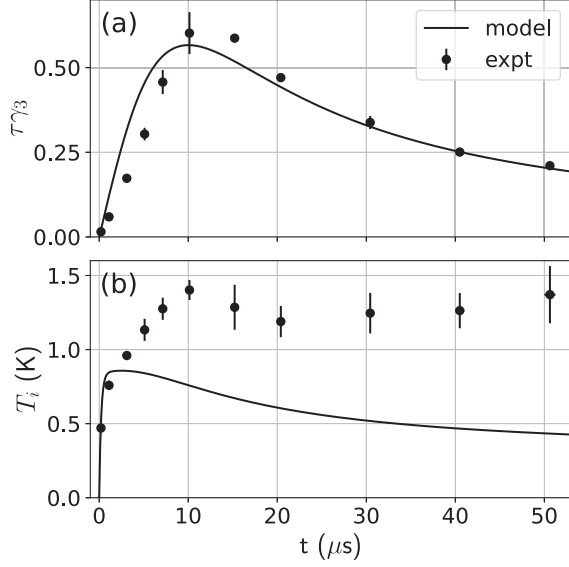
FIG. 2. Longitudinal UNP expansion in the presence of a magnetic field. The probe laser beam propagates in the z direction, parallel to $\vec{B}$. Black circles: experimental measurements. Error bars indicate 1σ scatter in repeated measurements. Solid line: one-dimensional expansion model. (a) The scaled hydrodynamic velocity gradient along the magnetic field direction, $\tau\gamma_3(t)$, agrees qualitatively with the asymmetric expansion model. There is no evidence of any oscillation in γ_3. (b) The ion temperature, T_i, reveals an additional source of heating beyond disorder-induced heating and electron-ion collisions in Eq. (A2). For this figure, $n_0 = 3.3(2) \times 10^8$ cm^{-3}, $\sigma_0 = 1.30$ mm, $T_e = 96$ K, and $B = 216$ G.

the earliest-time measurement in Fig. 2, it quickly becomes negative and oscillates around zero.

A study of ion acoustic waves in Refs. [87,88] showed that the hydrodynamic velocity of an ion acoustic standing wave can be written

$$u_{\text{IAW}} = A_0 \frac{\omega}{k} \exp(-\Gamma t) \sin(kx) \sin(\omega t), \quad (26)$$

where $k = 2\pi/\lambda$ is k vector associated with a wave of wavelength λ, $A_0\omega/k$ is the wave amplitude, and Γ is the damping rate. In this model, the undamped velocity gradient in the
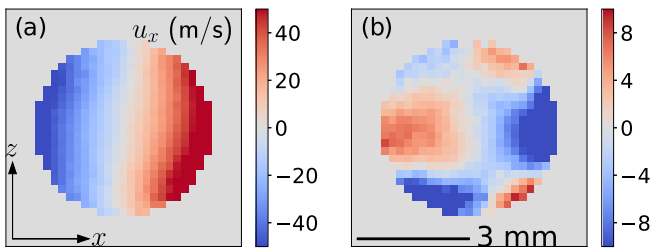

FIG. 3. Transverse hydrodynamic velocity measurements. (a) $B = 0$ and (b) $B = 183$ G. The initial electron temperature, ion density, and rms plasma size are $T_e = 100$ K, $n_0 = 6.7 \times 10^8$ cm^{-3}, and $\sigma_0 = 1.3$ mm. These show the hydrodynamic velocity 2 μs after the plasma was formed. The magnetic field points in the z direction, and the probe laser propagates in the $+x$ direction, from left to right.
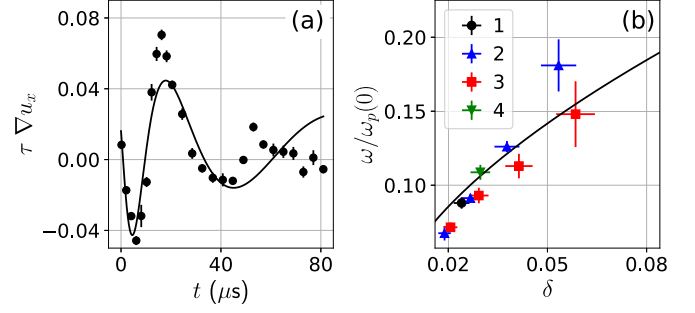

FIG. 4. (a) Scaled transverse velocity gradient in the presence of a magnetic field. In contrast to the longitudinal gradient plotted in Fig. 2, pronounced oscillations about zero are observed. The black circles are the experimental data. The solid line is a fit from Eq. (29). (b) Fitted scaled oscillation frequency vs charge imbalance. The symbols are experimental data with conditions listed in Table I. The solid line indicates the scaled ion plasma frequency at the edge of the electron density distribution, where the plasma becomes non-neutral.

center of the plasma is

$$\frac{\partial u_x}{\partial x} = A_0 \omega \sin(\omega t). \quad (27)$$

The one-dimensional plasma expansion of Sec. III predicts that the plasma frequency should fall according to

$$\omega_p(t) = \frac{\omega_p(0)}{(1 + t^2/\tau^2)^{1/4}} \quad (28)$$

as the plasma expands.

We fit the plasma velocity gradient oscillations in Fig. 4 to the function

$$\frac{\partial u_x}{\partial x} = \frac{a}{(1 + t^2/\tau^2)^{1/4}} \sin\left[b \frac{t/\tau}{(1 + t^2/\tau^2)^{1/4}} + c\right] + d, \quad (29)$$

where a, b, c, and d are fit parameters for the amplitude, scaled frequency, phase, and offset in the oscillation. The scaled oscillation frequency is

$$\frac{\omega}{\omega_p(0)} = \frac{b}{\omega_p(0)\tau}. \quad (30)$$

TABLE I. Experimental parameters for data in Fig. 4. The number in parentheses following the density, rms size, charge imbalance, and scaled oscillation frequency are the estimated uncertainties in the last digit(s).

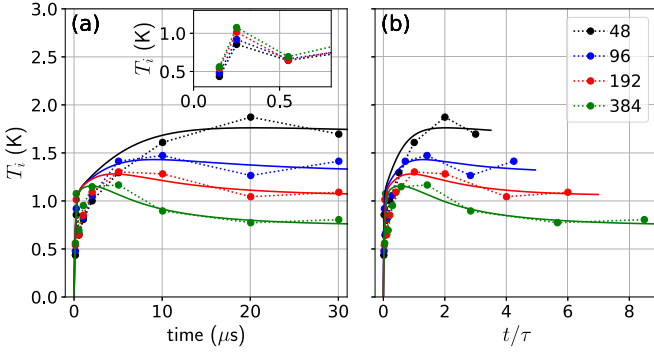|	B (G)	$T_e(0)$ (K)	n_0 (cm^{-3})	σ_0 (mm)	δ	$\omega/\omega_p(0)$
1	133	96	$4.6(5) \times 10^8$	1.3(1)	0.024(2)	0.088(4)
2	183	48	$6.7(7) \times 10^8$	1.0(1)	0.019(2)	0.067(5)
2	183	96	$6.7(7) \times 10^8$	1.0(1)	0.027(3)	0.091(2)
2	183	192	$6.7(7) \times 10^8$	1.0(1)	0.038(4)	0.126(4)
2	183	384	$6.7(7) \times 10^8$	1.0(1)	0.053(6)	0.181(18)
3	187	48	$3.3(3) \times 10^8$	1.3(1)	0.021(2)	0.072(3)
3	187	96	$3.3(3) \times 10^8$	1.3(1)	0.029(3)	0.093(5)
3	187	192	$3.3(3) \times 10^8$	1.3(1)	0.041(4)	0.113(8)
3	187	384	$3.3(3) \times 10^8$	1.3(1)	0.059(6)	0.148(22)
4	216	96	$3.2(3) \times 10^8$	1.3(1)	0.029(3)	0.109(5)

FIG. 5. Ion temperature for different initial electron temperatures. (a) As the initial electron temperature increases, the ion temperature decreases. The inset shows the ion temperature during the first 800 ns. (b) Plotting the ion temperature vs scaled time shows the influence of electron-ion collisions and plasma expansion. The legend shows initial electron temperatures in K. The circles and dashed lines show experimental data. Solid lines show predictions from the asymmetric expansion model of Sec. III with enhanced values of γ_{ei} as described in the text. The experimental temperature data are from set 2 in Fig. 4 and Table I.

The solid line in Fig. 4(a) shows the fit of this model to the data. While good, the agreement between the model and the experimental data is not perfect. The frequency chirp, which arises from the falling ion density, is reproduced reasonably well. However, the experimental oscillation appears to damp out more quickly than the model predicts. This discrepancy may arise from a transient response, not included in the standing wave model, or from imperfect initial conditions.

In Fig. 4(b) we plot the fitted scaled oscillation frequency as a function of the charge imbalance. These data were collected for experimental conditions spanning a factor of two in density, a factor of 8 in initial electron temperature and a factor of 1.6 in magnetic field strength (see Table I). Also plotted in Fig. 4(b) is the ion plasma frequency at the edge of the electron distribution, where the plasma becomes non-neutral. The fitted oscillation frequency appears to correspond to the ion plasma frequency at this location.

VI. THE ION TEMPERATURE

The ion temperature is plotted in Fig. 5 for a range of different initial electron temperatures. The circles and dotted lines show the experimental data. The solid lines show the results from the asymmetric expansion model of Sec. III with a small multiplicative adjustment to γ_{ei} used as a fit parameter. In Fig. 5(a), the temperature is plotted vs time. The inset shows the temperature during the first 800 ns. Although only partially resolved in the inset, the disorder-induced heating temperatures show the expected trend with electron temperature [89,90]. Smaller values of T_e correspond to shorter electron screening lengths. This, in turn, reduces the ion temperature while the system evolves from a completely disordered gas ($g_{ii} = 1$) towards a Yukawa liquid.

At times beyond 5 μs, the effects of electron temperature become manifest. The T_i trend in Fig. 5 is consistent with electron-ion heating. Smaller values of T_e correspond to

greater values of the electron-ion collision rate, as indicated in Eq. (A2).

Plotting the temperature data vs scaled expansion time [Fig. 5(b)] shows the influence of both electron-ion collisions and plasma expansion. For the model to better match the experimental data in this plot, the value of γ_{ei} has been increased by roughly a factor of 4. The difference between the model and the experimental temperatures is minimized for times $t \geqslant 10$ μs if γ_{ei} is increased by factors of [3.28, 3.53, 4.36, 4.69] for $T_e(0) = [48, 96, 192, 384]$ K. Our model evaluated γ_{ei} using the peak ion plasma density. If, instead, we had used the average plasma density, then the enhancement factors would need to be increased by an additional factor of $8^{1/2} \approx 3$. While these adjustments to γ_{ei} improve the late-time agreement, the model overestimates the ion temperature at early times. A simple multiplicative factor cannot bring the model into agreement with the experimental data for all measurements. Because of this, the quoted enhancement factors have low reliability, not because the fits are poor, but because the collision model appears to be missing important physics.

Generalizing the Coulomb logarithm in Eq. (A2) to include magnetic field effects has been discussed in many publications (see, for example, Refs. [26,27,91]). However, in Ref. [26] it is shown that the effect of a magnetic field is to reduce the Coulomb logarithm, contrary to what our simplified analysis suggests. It may be that the excess ion temperature is not due directly to the collision rate. It could result from excess electric field energy in the initial plasma state relative to equilibrium. Excess ion temperature was also observed in Ref. [58] for UNPs expanding without a magnetic field.

It has been suggested that an enhancement in the electron-ion collision rate exists when the electron plasma frequency equals the electron cyclotron frequency [92]. For the data in Fig. 5, the electron cyclotron frequency $\omega_c = eB/m_e = 3.8 \times 10^9$ s^{-1} and the electron plasma frequency $\omega_p^{(e)} = [(ne^2)/(m_e\epsilon_0)]^{1/2} = 1.5 \times 10^9$ s are comparable. However, the suggested collision rate enhancement has no electron temperature dependence, contrary to what we observe. Besides, the enhancement predicted in Ref. [92] is too small to account for the increases in γ_{ei} that we measure.

VII. CONCLUSION

In this paper we present a study of hydrodynamic velocity and ion temperature evolution in a strongly coupled, partially magnetized UNP. Although the density profile in the transverse direction is Gaussian [42,55], the ion velocity distribution displays rich dynamics. In Fig. 3 we show the presence of a low-frequency ion acoustic wave, giving rise to a shear velocity gradient in this strongly coupled plasma. In Fig. 4, we show that the frequency of this wave scales with the plasma charge imbalance consistent with the ion plasma frequency at the edge of the plasma, where the plasma becomes non-neutral. The exact nature of this response is the subject of future work. In Fig. 5 we show excess ion temperature relative to an expansion model. The excess temperature is consistent with electron-ion heating. However, the apparently enhanced value of γ_{ei} remains an open question.

Future work is needed to understand the electron-ion collision thermalization rate in the presence of a magnetic field.

The expansion dynamics, density gradients, and extended timescales in our system pose challenges for comparison to both theory and explicit electron molecular dynamics simulations. In the future, it may be possible to manipulate the electron-ion collision rate through electron cyclotron heating [93–96]. If successful in UNPs, then this heating could be a tool for manipulating the charge neutrality of the plasma, the eigenmode frequency, and, perhaps, the ion strong coupling parameter.

Future work could also explore mode excitation dynamics. In Eq. (27) we model the mode frequency as though it is a single frequency. In reality, many different modes are undoubtedly excited. The impulse response of the plasma [97] and its relaxation to a quasi-steady-state oscillation could be instructive. The visibility of modes as shown in Figs. 3 and 4 depends sensitively on the symmetry of the initial plasma. These modes therefore provide a way to probe the spatial density distribution. Future work using different geometries, those that provide a higher mode frequency compared to the plasma expansion rate, for example, would also allow measurements of the mode relaxation rate.

Plasma mixtures provide yet another rich avenue of future research [50,51,57,98]. Because the transverse modes are driven by non-neutrality at the edge of the plasma, it may be possible to excite transverse modes in different species, somewhat independently of the other, and to measure the approach to equilibrium.

APPENDIX: SUPPORTING EQUATIONS FOR SEC. III

Equations (14), (18) (22), and (23) form a set of coupled ordinary differential equations describing the plasma expansion. Solving these equations requires several additional equations. We include equations from Refs. [79] and [58] for γ_{ei} and U_{ii}.

$$\tau_{\text{corr}} = \sqrt{\frac{m_i \varepsilon_0}{n_i e^2}} = \left[\omega_p^{(i)}\right]^{-1}, \tag{A1}$$

$$\gamma_{ei} = \sqrt{\frac{2}{3\pi}} \Gamma_e^{3/2} \omega_{pe} \ln\left[1 / \left(\Gamma_e^{3/2} \sqrt{3}\right)\right], \tag{A2}$$

$$U_{ii,\text{eq}} = k_B T_i \Gamma_i^{3/2} \left(\frac{A_1}{\sqrt{A_2 + \Gamma_i}} + \frac{A_3}{1 + \Gamma_i}\right), \tag{A3}$$

$$\Gamma_i = \frac{e^2}{4\pi \varepsilon_0 a_{\text{ws}}} \frac{1}{k_B T_i}, \tag{A4}$$

$$\Gamma_e = \frac{e^2}{4\pi \varepsilon_0 a_{\text{ws}}} \frac{1}{k_B T_e}, \tag{A5}$$

$$\omega_{pe} = \sqrt{\frac{n_e e^2}{m_e \varepsilon_0}}, \tag{A6}$$

$$n_e = n_i = \frac{N_i}{(2\pi)^{3/2} \sigma_1 \sigma_2 \sigma_3}, \tag{A7}$$

$$a_{\text{ws}} = \left(\frac{3}{4\pi n_i}\right), \tag{A8}$$

$$A_1 = -0.9052, \tag{A9}$$

$$A_2 = 0.6322, \tag{A10}$$

$$A_3 = -\frac{\sqrt{3}}{2} - \frac{A_1}{\sqrt{A_2}} = 0.2724. \tag{A11}$$

[1] N. Sato, Existence of weakly quasisymmetric magnetic fields without rotational transform in asymmetric toroidal domains, Sci. Rep. **12**, 11322 (2022).

[2] M. Landreman and E. Paul, Magnetic fields with precise quasisymmetry for plasma confinement, Phys. Rev. Lett. **128**, 035001 (2022).

[3] J. Y. Kim, J. Y. Jang, J. Choi, J.-i. Wang, W. I. Jeong, M. A. I. Elgarhy, G. Go, K.-J. Chung, and Y. S. Hwang, Magnetic confinement and instability in partially magnetized plasma, Plasma Sourc. Sci. Technol. **30**, 025011 (2021).

[4] D. Yager-Elorriaga, M. Gomez, D. Ruiz, S. Slutz, A. Harvey-Thompson, C. Jennings, P. Knapp, P. Schmit, M. Weis, T. Awe, G. Chandler, M. Mangan, C. Myers, J. Fein, B. Galloway, M. Geissel, M. Glinsky, S. Hansen, E. Harding, D. Lamppa et al., An overview of magneto-inertial fusion on the Z machine at sandia national laboratories, Nucl. Fusion **62**, 042015 (2022).

[5] G. M. Gorman, M. K. Warrens, S. J. Bradshaw, and T. C. Killian, Magnetic confinement of an ultracold neutral plasma, Phys. Rev. Lett. **126**, 085002 (2021).

[6] H. Kählert, A. Melzer, M. Puttscher, T. Ott, and M. Bonitz, Magnetic fieldeffects and waves in complex plasmas, Eur. Phys. J. D **72**, 83 (2018).

[7] D. Bhattacharya, Formation and evolution of binary and millisecond radio pulsars, Phys. Rep. **203**, 1 (1991).

[8] R. C. Duncan and C. Thompson, Formation of very strongly magnetized neutron stars—Implications for gamma-ray bursts, Astrophys. J. **392**, L9 (1992).

[9] E. L. Clark, K. Krushelnick, J. R. Davies, M. Zepf, M. Tatarakis, F. N. Beg, A. Machacek, P. A. Norreys, M. I. K. Santala, I. Watts, and A. E. Dangor, Measurements of energetic proton transport through magnetized plasma from intense laser interactions with solids, Phys. Rev. Lett. **84**, 670 (2000).

[10] S. E. Woosley, Pulsational pair-instability supernovae, Astrophys. J. **836**, 244 (2017).

[11] J. L. Burch, T. E. Moore, R. B. Torbert, and B. L. Giles, Magnetospheric multiscale overview and science objectives, Space Sci. Rev. **199**, 5 (2016).

[12] F. H. Séguin, C. K. Li, M. J.-E. Manuel, H. G. Rinderknecht, N. Sinenian, J. A. Frenje, J. R. Rygg, D. G. Hicks, R. D. Petrasso, J. Delettrez, R. Betti, F. J. Marshall, and V. A. Smalyuk, Time evolution of filamentation and self-generated fields in the coronae of directly driven inertial-confinement fusion capsules, Phys. Plasmas **19**, 012701 (2012).

[13] R. S. Craxton, K. S. Anderson, T. R. Boehly, V. N. Goncharov, D. R. Harding, J. P. Knauer, R. L. McCrory, P. W. McKenty, D. D. Meyerhofer, J. F. Myatt, A. J. Schmitt, J. D. Sethian, R. W. Short, S. Skupsky, W. Theobald, W. L. Kruer, K. Tanaka, R. Betti, T. J. B. Collins, J. A. Delettrez *et al.*, Direct-drive inertial confinement fusion: A review, Phys. Plasmas **22**, 110501 (2015).

[14] D. Verscharen, K. G. Klein, and B. A. Maruca, The multiscale nature of the solar wind, Living Rev. Sol. Phys. **16**, 5 (2019).

[15] A. H. Boozer, Physics of magnetically confined plasmas, Rev. Mod. Phys. **76**, 1071 (2005).

[16] S. A. Slutz and R. A. Vesey, High-gain magnetized inertial fusion, Phys. Rev. Lett. **108**, 025003 (2012).

[17] M. R. Gomez, S. A. Slutz, C. A. Jennings, D. J. Ampleford, M. R. Weis, C. E. Myers, D. A. Yager-Elorriaga, K. D. Hahn, S. B. Hansen, E. C. Harding, A. J. Harvey-Thompson, D. C. Lamppa, M. Mangan, P. F. Knapp, T. J. Awe, G. A. Chandler, G. W. Cooper, J. R. Fein, M. Geissel, M. E. Glinsky *et al.*, Performance scaling in magnetized liner inertial fusion experiments, Phys. Rev. Lett. **125**, 155002 (2020).

[18] J. Ongena, R. Koch, R. Wolf, and H. Zohm, Magnetic-confinement fusion, Nat. Phys. **12**, 398 (2016).

[19] F. Wechsung, M. Landreman, A. Giuliani, A. Cerfon, and G. Stadler, Precise stellarator quasi-symmetry can be achieved with electromagnetic coils, Proc. Natl. Acad. Sci. USA **119**, (2022).

[20] X. Garbet, L. Garzotti, P. Mantica, H. Nordman, M. Valovic, H. Weisen, and C. Angioni, Turbulent particle transport in magnetized plasmas, Phys. Rev. Lett. **91**, 035001 (2003).

[21] J. A. Krommes, Fundamental statistical descriptions of plasma turbulence in magnetic fields, Phys. Rep. **360**, 1 (2002).

[22] J. Cho and E. T. Vishniac, The generation of magnetic fields through driven turbulence, Astrophys. J. **538**, 217 (2000).

[23] J. L. Burch, R. B. Torbert, T. D. Phan, L.-J. Chen, T. E. Moore, R. E. Ergun, J. P. Eastwood, D. J. Gershman, P. A. Cassak, M. R. Argall, S. Wang, M. Hesse, C. J. Pollock, B. L. Giles, R. Nakamura, B. H. Mauk, S. A. Fuselier, C. T. Russell, R. J. Strangeway, J. F. Drake *et al.*, Electron-scale measurements of magnetic reconnection in space, Science **352**, (2016).

[24] J. V. Hollweg, Kinetic Alfvén wave revisited, J. Geophys. Res.: Space Phys. **104**, 14811 (1999).

[25] N. Iwamoto, Collective modes in nonrelativistic electron-positron plasmas, Phys. Rev. E **47**, 604 (1993).

[26] D. K. Geller and J. C. Weisheit, Classical electron-ion scattering in strongly magnetized plasmas. I. A generalized coulomb logarithm, Phys. Plasmas **4**, 4258 (1997).

[27] Y. T. Lee and R. M. More, An electron conductivity model for dense plasmas, Phys. Fluids **27**, 1273 (1984).

[28] W. Horton, Drift waves and transport, Rev. Mod. Phys. **71**, 735 (1999).

[29] F. L. Hinton and R. D. Hazeltine, Theory of plasma transport in toroidal confinement systems, Rev. Mod. Phys. **48**, 239 (1976).

[30] X.-N. Bai and J. M. Stone, Effect of ambipoloar diffusion on the nonlinear evolution of magnetorotational instability in weakly ionized disks, Astrophys. J. **736**, 144 (2011).

[31] H. Kählert, G. J. Kalman, and M. Bonitz, Dynamics of strongly correlated and strongly inhomogeneous plasmas, Phys. Rev. E **90**, 011101(R) (2014).

[32] T. Ott, M. Bonitz, and Z. Donkó, Effect of correlations on heat transport in a magnetized strongly coupled plasma, Phys. Rev. E **92**, 063105 (2015).

[33] T. Ott, M. Bonitz, P. Hartmann, and Z. Donkó, Spontaneous generation of temperature anisotropy in a strongly coupled magnetized plasma, Phys. Rev. E **95**, 013209 (2017).

[34] T. Ott and M. Bonitz, Diffusion in a strongly coupled magnetized plasma, Phys. Rev. Lett. **107**, 135003 (2011).

[35] Y. Feng, J. Goree, B. Liu, T. P. Intrator, and M. S. Murillo, Superdiffusion of two-dimensional yukawa liquids due to a perpendicular magnetic field, Phys. Rev. E **90**, 013105 (2014).

[36] Y. Feng, W. Lin, and M. S. Murillo, Viscosity of two-dimensional strongly coupled dusty plasma modified by a perpendicular magnetic field, Phys. Rev. E **96**, 053208 (2017).

[37] Q. Wargnier, A. A. Laguna, J. B. Scoggins, N. N. Mansour, M. Massot, and T. E. Magin, Consistent transport properties in multicomponent two-temperature magnetized plasmas, Astron. Astrophys. **635**, A87 (2020).

[38] L. Jose and S. D. Baalrud, A kinetic model of friction in strongly coupled strongly magnetized plasmas, Phys. Plasmas **28**, 072107 (2021).

[39] L. Jose and S. D. Baalrud, Theory of the ion–electron temperature relaxation rate in strongly magnetized plasmas, Phys. Plasmas **30**, 052103 (2023).

[40] S. K. Tiwari and S. D. Baalrud, Reduction of electron heating by magnetizing ultracold neutral plasma, Phys. Plasmas **25**, 013511 (2018).

[41] K. R. Vidal and S. D. Baalrud, Extended space and time correlations in strongly magnetized plasmas, Phys. Plasmas **28**, 042103 (2021).

[42] R. T. Sprenkle, S. D. Bergeson, L. G. Silvestri, and M. S. Murillo, Ultracold neutral plasma expansion in a strong uniform magnetic field, Phys. Rev. E **105**, 045201 (2022).

[43] P. E. Grabowski Jr., S. Hansen, M. Murillo, L. Stanton, F. Graziani, A. Zylstra, S. Baalrud, P. Arnault, A. Baczewski, L. Benedict, C. Blancard, O. Čertík, J. Clérouin, L. Collins, S. Copeland, A. Correa, J. Dai, J. Daligault, M. Desjarlais, M. Dharma-wardana *et al.*, Review of the first charged-particle transport coefficient comparison workshop, High Energy Density Phys. **37**, 100905 (2020).

[44] V. S. Dharodi and M. S. Murillo, Sculpted ultracold neutral plasmas, Phys. Rev. E **101**, 023207 (2020).

[45] T. Killian, T. Pattard, T. Pohl, and J. Rost, Ultracold neutral plasmas, Phys. Rep. **449**, 77 (2007).

[46] M. Lyon and S. L. Rolston, Ultracold neutral plasmas, Rep. Prog. Phys. **80**, 017001 (2017).

[47] T. K. Langin, G. M. Gorman, and T. C. Killian, Laser cooling of ions in a neutral plasma, Science **363**, 61 (2019).

[48] M. Lyon, S. D. Bergeson, A. Diaw, and M. S. Murillo, Using higher ionization states to increase coulomb coupling in an ultracold neutral plasma, Phys. Rev. E **91**, 033101 (2015).

[49] S. D. Bergeson, S. D. Baalrud, C. L. Ellison, E. Grant, F. R. Graziani, T. C. Killian, M. S. Murillo, J. L. Roberts, and L. G. Stanton, Exploring the crossover between high-energy-density plasma and ultracold neutral plasma physics, Phys. Plasmas **26**, 100501 (2019).

[50] R. T. Sprenkle, L. G. Silvestri, M. S. Murillo, and S. D. Bergeson, Temperature relaxation in strongly-coupled binary ionic mixtures, Nat. Commun. **13**, 15 (2022).

[51] L. G. Silvestri, R. T. Sprenkle, S. D. Bergeson, and M. M. Murillo, Relaxation of strongly coupled binary ionic mixtures in the coupled mode regime, Phys. Plasmas **28**, 062302 (2021).

[52] E. V. Crockett, R. C. Newell, F. Robicheaux, and D. A. Tate, Heating and cooling of electrons in an ultracold neutral plasma using Rydberg atoms, Phys. Rev. A **98**, 043431 (2018).

[53] M. A. Viray, S. A. Miller, and G. Raithel, Coulomb expansion of a cold non-neutral rubidium plasma, Phys. Rev. A **102**, 033303 (2020).

[54] T. Kroker, M. Großmann, K. Sengstock, M. Drescher, P. Wessels-Staarmann, and J. Simonet, Ultrafast electron cooling in an expanding ultracold plasma, Nat. Commun. **12**, 596 (2021).

[55] X. L. Zhang, R. S. Fletcher, S. L. Rolston, P. N. Guzdar, and M. Swisdak, Ultracold plasma expansion in a magnetic field, Phys. Rev. Lett. **100**, 235002 (2008).

[56] L. G. Stanton, S. D. Bergeson, and M. S. Murillo, Transport in non-ideal, multi-species plasmas, Phys. Plasmas **28**, 050401 (2021).

[57] T. Sprenkle, A. Dodson, E. McKnight, R. Spencer, S. Bergeson, A. Diaw, and M. S. Murillo, Ion friction at small values of the Coulomb logarithm, Phys. Rev. E **99**, 053206 (2019).

[58] P. McQuillen, T. Strickler, T. Langin, and T. C. Killian, Ion temperature evolution in an ultracold neutral plasma, Phys. Plasmas **22**, 033513 (2015).

[59] G. Bannasch, J. Castro, P. McQuillen, T. Pohl, and T. C. Killian, Velocity relaxation in a strongly coupled plasma, Phys. Rev. Lett. **109**, 185008 (2012).

[60] T. S. Strickler, T. K. Langin, P. McQuillen, J. Daligault, and T. C. Killian, Experimental measurement of self-diffusion in a strongly coupled plasma, Phys. Rev. X **6**, 021021 (2016).

[61] W.-T. Chen, C. Witte, and J. L. Roberts, Observation of a strong-coupling effect on electron-ion collisions in ultracold plasmas, Phys. Rev. E **96**, 013203 (2017).

[62] P. Jiang and J. L. Roberts, Electric field influences on the initial electron temperature of ultracold plasmas, Phys. Plasmas **26**, 043513 (2019).

[63] M. Aghigh, K. Grant, R. Haenel, K. L. Marroquín, F. B. V. Martins, H. Sadegi, M. Schulz-Weiling, J. Sous, R. Wang, J. S. Keller, and E. R. Grant, Dissipative dynamics of atomic and molecular Rydberg gases: Avalanche to ultracold plasma states of strong coupling, J. Phys. B: At., Mol. Opt. Phys. **53**, 074003 (2020).

[64] J. Sous and E. Grant, Possible many-body localization in a long-lived rinite-temperature ultracold quasineutral molecular plasma, Phys. Rev. Lett. **120**, 110601 (2018).

[65] K. A. Twedt and S. L. Rolston, Radio-frequency detection of electron oscillations in ultracol plasmas, Bull. Am. Phys. Soc. **56** (2011).

[66] J. M. Guthrie and J. L. Roberts, Finite-amplitude RF heating rates for magnetized electrons in neutral plasma, Phys. Plasmas **28**, 052101 (2021).

[67] G. M. Gorman, M. K. Warrens, S. J. Bradshaw, and T. C. Killian, Laser-induced-fluorescence imaging of a spin-polarized ultracold neutral plasma in a magnetic field, Phys. Rev. A **105**, 013108 (2022).

[68] S. Y. Bronin, E. V. Vikhrov, B. B. Zelener, and B. V. Zelener, Physical processes underlying the formation of a steady-state ultracold nonideal plasma, JETP Lett. **114**, 572 (2021).

[69] S. Y. Bronin, E. V. Vikhrov, B. B. Zelener, and B. V. Zelener, Magnetic field effect on the formation of ultracold plasma, JETP Lett. **117**, 116 (2023).

[70] P. Steinbrunner, T. O'Neil, M. Stoneking, and D. Dubin, Thermal equilibrium of collisional non-neutral plasma in a magnetic dipole trap, J. Plasma Phys. **89**, 935890401 (2023).

[71] D. H. E. Dubin and T. M. O'Neil, Trapped nonneutral plasmas, liquids, and crystals (the thermal equilibrium states), Rev. Mod. Phys. **71**, 87 (1999).

[72] F. Anderegg, N. Shiga, J. R. Danielson, D. H. E. Dubin, C. F. Driscoll, and R. W. Gould, Thermally excited modes in a pure electron plasma, Phys. Rev. Lett. **90**, 115001 (2003).

[73] M. Puttscher Jr., A. Melzer, U. Konopka, S. LeBlanc, B. Lynch, and E. Thomas, Vertical oscillations of dust particles in a strongly magnetized plasma sheath induced by horizontal laser manipulation, Phys. Plasmas **24**, 013701 (2017).

[74] A. Lyubonko, T. Pohl, and J.-M. Rost, Collective energy absorption of ultracold plasmas through electronic edge-modes, New J. Phys. **14**, 053039 (2012).

[75] T. C. Killian, S. Kulin, S. D. Bergeson, L. A. Orozco, C. Orzel, and S. L. Rolston, Creation of an ultracold neutral plasma, Phys. Rev. Lett. **83**, 4776 (1999).

[76] S. D. Bergeson and R. L. Spencer, Neutral-plasma oscillations at zero temperature, Phys. Rev. E **67**, 026414 (2003).

[77] R. S. Fletcher, X. L. Zhang, and S. L. Rolston, Observation of collective modes of ultracold plasmas, Phys. Rev. Lett. **96**, 105003 (2006).

[78] D. S. Dorozhkina and V. E. Semenov, Exact solution of vlasov equations for quasineutral expansion of plasma bunch into vacuum, Phys. Rev. Lett. **81**, 2691 (1998).

[79] T. Pohl, T. Pattard, and J. M. Rost, Kinetic modeling and molecular dynamics simulation of ultracold neutral plasmas including ionic correlations, Phys. Rev. A **70**, 033416 (2004).

[80] E. A. Cummings, J. E. Daily, D. S. Durfee, and S. D. Bergeson, Ultracold neutral plasma expansion in two dimensions, Phys. Plasmas **12**, 123501 (2005).

[81] M. Mills, P. Puri, Y. Yu, A. Derevianko, C. Schneider, and E. R. Hudson, Efficient repumping of a ca magneto-optical trap, Phys. Rev. A **96**, 033402 (2017).

[82] For some of the data, we probe the ions using the 397 nm $^2S_{1/2}$ - $^2P_{1/2}$ transition.

[83] T. K. Langin, T. Strickler, N. Maksimovic, P. McQuillen, T. Pohl, D. Vrinceanu, and T. C. Killian, Demonstrating universal scaling for dynamics of Yukawa one-component plasmas after an interaction quench, Phys. Rev. E **93**, 023201 (2016).

[84] See Supplemental Material at http://link.aps.org/supplemental/10.1103/PhysRevE.109.015201 for optical imaging analysis.

[85] J. Peatross and M. Ware, *Physics of Light and Optics*, 2nd ed. (McGraw-Hill Education, New York, 2015).

[86] J. Jin and D. A. Church, Excited-level lifetimes and hyperfine-structure measurements on ions using collinear laser–ion-beam spectroscopy, Phys. Rev. A **49**, 3463 (1994).

[87] J. Castro, P. McQuillen, and T. C. Killian, Ion acoustic waves in ultracold neutral plasmas, Phys. Rev. Lett. **105**, 065004 (2010).

[88] T. C. Killian, P. McQuillen, T. M. O'Neil, and J. Castro, Creating and studying ion acoustic waves in ultracold neutral plasmas, Phys. Plasmas **19**, 055701 (2012).

[89] M. Lyon and S. D. Bergeson, The influence of electron screening on disorder-induced heating, J. Phys. B: At., Mol. Opt. Phys. **44**, 184014 (2011).

[90] M. Lyon, S. D. Bergeson, and M. S. Murillo, Limit of strong ion coupling due to electron shielding, Phys. Rev. E **87**, 033101 (2013).

[91] S. A. Koryagin, Electron-ion collision integral in a strong magnetic field, J. Exp. Theor. Phys. **90**, 741 (2000).

[92] I. L. Isaev and A. P. Gavriliuk, Interaction of ultracold non-ideal ion–electron plasma with a uniform magnetic field, J. Phys. B: At., Mol. Opt. Phys. **51**, 025701 (2018).

[93] R. Prater, Heating and current drive by electron cyclotron waves, Phys. Plasmas **11**, 2349 (2004).

[94] P. W. Smorenburg, L. P. J. Kamp, and O. J. Luiten, Heating mechanisms in radio-frequency-driven ultracold plasmas, Phys. Rev. A **85**, 063413 (2012).

[95] M. A. W. van Ninhuijs, K. A. Daamen, J. G. H. Franssen, J. Conway, B. Platier, J. Beckers, and O. J. Luiten, Microwave cavity resonance spectroscopy of ultracold plasmas, Phys. Rev. A **100**, 061801(R) (2019).

[96] M. Thumm, State-of-the-art of high-power gyro-devices and free electron masers, J. Infrar. Millimeter Terahertz Waves **41**, 1 (2020).

[97] T. M. Wilson, W.-T. Chen, and J. L. Roberts, Density-dependent response of an ultracold plasma to few-cycle radio-frequency pulses, Phys. Rev. A **87**, 013410 (2013).

[98] T. Ott, H. Löwen, and M. Bonitz, Dynamics of two-dimensional one-component and binary yukawa systems in a magnetic field, Phys. Rev. E **89**, 013105 (2014).